Digital removal of autofluorescence from microscopy images

Heeva Baharlou[1,2]*, Nicolas P Canete[1,2]*, Kirstie M Bertram[1,2], Kerrie J Sandgren[1,2], Anthony L Cunningham[1,2], Andrew N Harman[1,2†], Ellis Patrick[1,2†§]

1. Centre for Virus Research, The Westmead Institute for Medical Research, 176 Hawkesbury Road, Westmead, NSW 2145 Australia
2. The University of Sydney, Sydney, Australia

*,† equal contribution, § corresponding author

Abstract:

Autofluorescence is a long-standing problem that has hindered fluorescence microscopy image analysis. To address this, we have developed a method that identifies and removes autofluorescent signals from multi-channel images post acquisition. We demonstrate the broad utility of this algorithm in accurately assessing protein expression *in situ* through the removal of interfering autofluorescent signals.

Availability and implementation: https://ellispatrick.github.io/AFremover
Contact: ellis.patrick@sydney.edu.au
Supplementary information: Supplementary Figs. 1-13

Immunofluorescence microscopy (IF) is a powerful tool for simultaneously visualising the localisation of multiple proteins *in situ*. Additionally, several methods have been developed that push the number of parameters visualised in a single section to well beyond traditional 3-4 colour IF[1–7]. This allows for the definition of multiple cell types, complex subsets, and also cellular states *in situ.* Despite these advances the utility of IF, particularly in the clinical setting, has been hampered by the longstanding issue of autofluorescence.

Autofluorescence is present in all tissues and has many sources including components of structural and connective tissues, cellular cytoplasmic contents and also fixatives used to preserve tissue [8–11]. Autofluorescent substances have their own excitation and emission profiles that can span the entire visible and even infra-red spectrum and therefore significantly overlap with standard microscope excitation/emission filter setups[10] **(Supplementary Fig. 1**). This presents a major obstacle to image analysis, particularly any kind of automated analyses, as 'real' vs 'autofluorescent' regions of interest (ROIs) cannot be readily distinguished. An example of this is shown (**Supplementary Fig. 2**) where the accurate quantification of CD3 labelling in human colon tissue is severely hampered by autofluorescent signals.

Several methods have been developed to address the issue of autofluorescence. The oldest and most widely used are chemical methods to quench autofluorescence. These include exposing samples to either UV radiation or a chemical solution prior to or during staining[9,12–14]. Although these methods can be effective, there are several disadvantages including quenching of desired signal from endogenous reporters or fluorescent probes, and also that

there is no general recipe with specific protocols required to quench specific types of autofluorescence [9,14]. However, the primary limitation is that the quenching must take place prior to imaging, so if autofluorescence is detected after image acquisition it is too late to remove it. This can be frustrating as autofluorescence is highly variable between tissue sections.

Digital methods of autofluorescence removal have also been developed such as spectral unmixing and algorithmic subtraction of a background reference image acquired prior to staining[2,15,16]. These methods are robust and have the capacity to resolve signal vs autofluorescence. However, they require specialised microscopes, considerable extra staining and imaging steps and also proprietary software. Importantly, these methods also need to be run at the time of image acquisition. These obstacles prevent generalised use. As such there is an urgent need for effective and open source methods to tackle the issue of autofluorescence after image acquisition.

Here we describe Autofluorescence Remover, a fast and effective method for automated detection of autofluorescent regions of interest (ROIs) in IF images of tissue. The algorithm requires only the information from two fluorescent channels, where bright fluorescent ROIs are located and classified as 'real' or 'autofluorescent' based on measures of pixel correlation, distribution and dynamic range. We then employ a novel dilation function that works to outline the full body of autofluorescent ROIs. A key advantage of this method is that it is applied to images post-acquisition and can therefore be used to filter existing image data sets.

The steps for the Autofluorescence Remover algorithm are summarised in **Fig. 1.** First, thresholds are applied to the two fluorescent channels and an 'intersection mask' is created to detect the ROIs that are fluorescing in both channels (**Fig. 1a, left**). Second, we then measure ROIs in the 'intersection mask' for multiple textural features **(Fig. 1a, middle)**. To select these features, we make a key assumption that the fundamental topology of pixel intensities for an autofluorescent ROI is conserved across channels. This makes sense as sources of autofluorescence tend to have long excitation and emission profiles. As such, any measure of pixel behaviour within an ROI will be linearly correlated across channels (**Supplementary Fig. 3a-c**). Therefore, to identify autofluorescence we measure multiple features including pixel correlation (Pearson's correlation coefficient), dynamic range (Standard Deviation) and distribution (Kurtosis). Third, ROIs can be clustered using the textural features as inputs to identify a distinct cluster with high correlation values that consists mainly of autofluorescent ROIs (**Fig. 1a, right**). Here we have used a *k*-means clustering algorithm with automated choice of *k*. Finally, these autofluorescent ROIs can be excluded from downstream analysis or can be subtracted from the raw images for visualisation (**Fig. 1b,c**).

For optimal visualisation, and to aid in downstream analysis, we have also developed a novel algorithm for removing the identified autofluorescence. Due to variations in intensity scale within an image and across different images, conventional thresholding algorithms rarely capture the correct perimeter of autofluorescent ROIs (**Supplementary Fig. 4a-c**). This can represent a limitation for automated autofluorescence removal, as several threshold parameters need to be tested beforehand for each image, and then assessed by eye to

determine appropriateness. To overcome this limitation we developed a custom dilation function that works in tandem with thresholding to automatically outline the full body of autofluorescent ROIs, regardless of shape and intensity (**Fig. 1c)**. In brief this works by skeletonising ROIs and evenly distributing points throughout the skeleton (**Supplementary Fig. 4d**). We then expand from these points until the gradient of pixel intensities from the ROI boundary outwards begins to increase, indicating the end of the object or the beginning of a neighbouring object (**Supplementary Fig. 4e**). We find that this method accurately captures the full perimeter of autofluorescent ROIs with minimal effect to neighbouring signals (**Supplementary Fig. 4f**). The final result is an image retaining only non-autofluorescent ROIs, which can then be used for visualisation and downstream analysis (**Fig. 1c**).

In order to establish both the efficacy and scope of utility for Autofluorescence Remover we tested the algorithm with multiple types of input images. First, we tested whether the markers for detection in each channel could influence autofluorescence identification. To this end we defined three use-cases where input channels contained (1) non-co-expressed markers (CD11c and CD3), (2) a marker expressed on autofluorescent cells (FXIIIA+ Macrophages) and (3) co-expressed markers (CD3 and CD4). These three use-cases are shown for human colorectal tissue where sections were imaged before (**Fig. 2a,d,g**) and after staining (**Fig. 2b,e,h**). The unstained image was used for manual annotation of autofluorescent ROIs providing a ground truth for our classifier, and not used in the removal process. We found that in all three use-cases the autofluorescence cluster was highly enriched for autofluorescent ROIs (mean =98.4%, SD = 1.6%, n=9). (**Supplementary Fig. 5a**). We also achieved good coverage identifying on average 96.0% (SD = 4.0%, n=9) of all annotated autofluorescence, with a low false positive rate of 1.7% (SD = 1.7%, n=9) (**Supplementary Fig. 5b**).
Pairwise plots for each use case are shown (**Supplementary Fig. 6-8**), demonstrating good separation of autofluorescence (yellow) from non-autofluorescence (grey) by *k*-means. The final result of autofluorescence removal, after applying the custom dilation function is shown (**Fig. 2c,f,i**), demonstrating near complete removal of autofluorescence in all three use cases.

We also show that Autofluorescence Remover successfully removes autofluorescence across various tissue-types, including heart, skin and brain tissues where autofluorescence is a well-known problem (**Supplementary Fig. 9**). Autofluorescence identification worked similarly across images of varying quality, including variations in resolution, (**Supplementary Fig. 10)** and on images both pre- and post- deconvolution (**Supplementary Fig. 11**). Further, our algorithm is compatible with very large images that are inundated with autofluorescence, which allows large data sets with significant noise to be rescued for analysis (**Supplementary Fig. 12**).

Finally, we show that the presence of autofluorescence and its removal can have a major impact on down-stream analysis. In our own studies, we are interested in the early HIV-target cell interactions that occur in human colorectal explants that we topically infect with HIV. However, these explants are prone to significant amounts of autofluorescence. To examine the localisation of HIV with CD11c+ cells we divide an image into 100x100um^2 quadrats and classify each as HIV- or HIV+ and then measure the density of CD11c labelling

in each area to quantify expression. Prior to autofluorescence removal, the apparent CD11c expression did not significantly differ between HIV- and HIV+ areas (**Fig. 3a**), whereas after removal CD11c expression was revealed as significantly higher in HIV+ areas compared to HIV- areas (**Fig. 3b**). This was due to a large amount of measured CD11c expression being derived from autofluorescence (**Fig. 3c)**. Further, we found that CD11c, HIV and autofluorescent cells were differentially located. CD11c and HIV clustered toward the tip of the lamina propria where the majority of interactions took place (**Fig. 3c, zoomed images**), whilst autofluorescent cells were particularly clustered toward the base of lamina propria, thus skewing the results. These data demonstrate the importance of autofluorescence removal to facilitate accurate image analysis.

Here we have presented a first of its kind method for the post-acquisition, automated detection and removal of autofluorescence in multi-channel images post-acquisition. This approach overcomes many of the limitations of existing methods that have prohibited their widespread use. Autofluorescence Remover is capable of removing autofluorescence that is stand-alone or nearby/touching non-autofluorescent signals. However, our approach does have limitations. It is unable to remove autofluorescence that mostly overlaps with a fluorescently stained object of interest. This can be an advantage in that stained cells of interest which exhibit autofluorescence are not removed, as shown for Macrophages in **Fig. 2**. Nevertheless, it does present limitations when precise measurements of fluorescent signals are required. Furthermore the algorithm requires that autofluorescent signals are present, even if only faintly, across at least two acquired channels. In our experience this was true of all bright interfering autofluorescence in the various tissues used for this study and fits in with the well-known broad spectra of autofluorescence[10]. However we cannot discount the possibility of specific types of autofluorescence having narrow emission profiles that might appear in only one channel. The diversity of biological samples means that no one approach can offer a complete solution. However, Autofluorescence Remover provides a major leap forward in extracting useful data from images plagued by autofluorescence by offering an approach that is easily incorporated into existing workflows in ImageJ, Matlab and R, and that can generalise to various samples, staining panels and image acquisition methods.

Methods:

Immunofluorescence staining. Tissues were fixed in 4% paraformaldehyde (Electron Microscopy Sciences) for 18-24h at room temperature then immersed in 70% ethanol prior to paraffin embedding. 4um paraffin sections were adhered to glass slides (SuperFrost Plus, Menzel Glazer), baked at 60°C for 40 min, dewaxed in xylene followed by 100% ethanol then air dried. All wash steps described herein were carried out by immersing slides in three successive Coplan Jars of Tris-buffered saline (Amresco, Cat: 0788) on a rotator for a total of 10 minutes. Antigen retrieval was then performed using a pH9 antigen retrieval buffer (DAKO) in a decloaking chamber (Biocare) for 20 min at 95°C. Slides were then washed in TBS. To acquire unlabelled background images (**Fig. 2, Supplementary Figs. 2 and 9**), sections were stained with 1ug/ml DAPI (Roche) for 3 minutes, mounted under coverslips with SlowFade-Diamond Antifade (Molecular Probes) and the whole section imaged on an Olympus VS120 microscope (see Image acquisition below). Coverslips were then floated

away in TBS and sections on slides were blocked for 30 min (0.1% saponin, 1% BSA, 10% donkey serum, diluted in TBS) at room temperature. Sections were then washed in TBS and incubated with primary antibodies overnight at 4°C. Antibodies for primary detection include: Abcam: - rabbit CD11c (EP1347Y), mouse CD3 (F7.2.38), rabbit CD8 (polyclonal, ab4055); DAKO – rabbit CD3 (polyclonal, A045229-2); Affinity Biologicals – sheep FXIIIA (polyclonal). Sections were then washed in TBS and incubated with secondary antibodies for 30min at room temperature. Donkey secondary antibodies (Molecular Probes) against rabbit, mouse or sheep were used and were conjugated to either Alexa Fluor 488 or 546. Sections were stained with DAPI (if not already performed in a previous step) and mounted with SlowFade-Diamond Antifade.

HIV explant infection. Healthy Inner foreskin explants were infected with either HIV_{Bal} or Transmitted/Founder HIV-1 Z3678M using an explant setup as previously described[17]. A $TCID_{50}$ of 3500 (titrated on TZMBLs as previously described[18]) was used to infect all explants. Tissues were then fixed and paraffin embedded as described above.

RNAScope. Detection of HIV RNA was performed using the 'RNAscope 2.5HD Reagent Kit-RED' and following the manufacturer's protocol (Cat: 322360, ACD Bio) with custom probes (consisting of 85 zz pairs) against HIV-1_{BaL} (REF: 486631, ACD Bio) spanning base pairs 1144-8431 of HIV-1_{BaL} sequence. Following the RNAscope protocol, sections were stained from the blocking step as detailed above.

Microscopy. Imaging was performed using an Olympus VS120 Slide Scanner with ORCA-FLASH 4.0 VS: Scientific CMOS camera. VS-ASW 2.9 Olympus software was used for acquisition of images and conversion of raw vsi files to tiff format for downstream processing. Objectives used are indicated in figure legends and include: x10 (UPLSAPO 10X/ NA 0.4, WD 3.1 / CG Thickness 0.17), x20 (UPLSAPO 20X/ NA 0.75, WD 0.6 / CG Thickness 0.17) and x40 (UPLSAPO 40X/ NA 0.95, WD 0.18 / CG Thickness 0.11–0.23). Channels used include: DAPI (Ex 387/11-25 nm; Em: 440/40-25 nm), FITC (Ex:485/20-25 nm; Em: 525/30-25 nm), TRITC (Ex:560/25-25 nm; Em: 607/36- 25 nm) and Cy5 (Ex: 650/13-25 nm; Em: 700/75-75 nm). For x40 images, Z-stacks were acquired 3.5um above and below the plane of focus with 0.5um step sizes. Huygens Professional 18.10 (Scientific Volume Imaging, The Netherlands, http://svi.nl) CMLE algorithm, with SNR:20 and 40 iterations, was used for deconvolution of Z-stacks. For images where the unstained background was acquired prior to staining, images were aligned using the ImageJ plugin multiStackReg vs1.45 with the DAPI channel serving as a reference for alignment.

Acquisition of Autofluorescence Spectra. Autofluorescence spectra of unstained tissue samples (**Supplementary Fig. 1**) were acquired using an Olympus FV1000 laser scanning confocal microscope with a x20 objective. The excitation lasers lines 405nm, 473nm and 559nm were used and emission spectra were acquired using a 20nm wide bandpass filter, shifted in 20nm intervals from 415-795nm, 490-790nm and 575-795nm respectively.

Generation of Intersection Mask. A mask of the intersection of the two channels was used for autofluorescence removal. This is termed the 'intersection mask'. The intersection mask contains only signals present in both channels and therefore contains the autofluorescent ROIs among other objects such as co-stained markers and dim background stromal

fluorescence. The intersection mask was generated by the following procedure. Each channel was Gaussian blurred with a sigma of 2. A Niblack threshold was then applied to each channel (threshold radius 30 pixels) to generate binary masks. The intersection ('AND' operation) of these masks was then taken and used for autofluorescence classification by clustering as detailed below.

Clustering for autofluorescence identification. Within the objects defined by the intersection mask we measured multiple features in each of the two channels on non-Gaussian blurred images. These features included standard deviation, kurtosis, as well as the inter-channel Pearson's correlation coefficient of corresponding pixels. These features were transformed by taking the natural log (standard deviation, skewness and kurtosis) or the inverse tanh transformation (correlation). All features were standardised by dividing by the standard deviation of the transformed feature values. *k*-means clustering was then performed on these features to identify a cluster of ROIs which are likely to be autofluorescent. The cluster with the highest average correlation value was defined as the cluster containing autofluorescent ROIs. A well-chosen number of clusters (*k*) is important for detecting a homogeneous cluster of autofluorescent ROIs. As such we developed an automated approach for optimal choice of *k* (high sensitivity and specificity). The procedure is as follows. 1. *k*-means is performed iteratively with 3-20 clusters 2. A two-tailed t-test is performed on the arctanh transformed correlation values of the two clusters with highest average correlation values. 3. The test statistic values are then plotted against *k*, which produces an asymptotically decreasing function (**Supplementary Fig. 13**). 4. We developed an 'elbow method' approach to finding the optimal cluster number. A straight line is drawn connecting the statistic value for the lowest *k*, to that of the highest *k*. The perpendicular distance of each plotted point to the line is measured and the optimal *k* is estimated to correspond to the point with the greatest distance below the line. This method is illustrated in (**Supplementary Fig. 13**). The intersection mask is then modified, keeping only the objects identified as autofluorescence.

Custom dilation thresholding to outline autofluorescent ROIs. After clustering and creating a mask of autofluorescent objects we then employed a custom dilation function to outline the full body of autofluorescent objects for removal. The essence of the algorithm is to evenly distribute points within an amorphous object and then to expand out from these points in all directions until a halting condition is met.
To distribute points the following approach was developed: 1. ROIs in the autofluorescence mask were skeletonised, reducing objects to a line of 1 pixel-width that follows the morphological gradient of the original object. 2. End-node pixels for each object in the image were first identified, defined as having only one neighbour. If there were no end-nodes for an object, as in the case of an annulus, the top-left-most pixel was defined as the end-node. 3. A skeleton tracing algorithm was employed that starts from the end nodes and moves throughout the skeleton, distributing centres for expansion every 20 pixels (illustrated in **Supplementary Fig. 4d**). Tracing of pixels to neighbours occurred as long as the neighbouring pixel was in the skeleton and had not yet been traced by another point. Once these conditions were no longer met, tracing for a given object was halted.
Expansion from distributed centres was carried out as follows: 1. Lines of length 60 pixels emanating from centres were drawn in all directions separated by an angle of theta where theta was defined by the law of cosines. 2. Pixel values of the Gaussian blurred image

for each channel were measured beginning from the point of intersection of the line and perimeter of the object in the intersection mask, to the end of the line. 3. The co-ordinates of the first point where pixel values increased were recorded for each line. 4. A new outline of the object was created by combining these co-ordinates (**Supplementary Fig. 4e**). 5. Pixel values of the new outline of the object were set to 0.

Algorithm performance assessment. The performance of our algorithm was tested using three different staining panels on human colonic tissue as shown in **Fig. 2**. To benchmark performance assessment, we manually annotated regions of the intersection mask (see 'Generation of Intersection Mask' above) as belonging to 'real' or 'autofluorescent' signals. Delineation of the two types of signal was achieved using the 'unstained background image' as a reference (see 'Immunofluorescent Staining' above). In total 400 ROIs, 200 for each category, were annotated. The actual annotation was performed using the Cell Counter Plugin in ImageJ. Results were exported as a csv file, where each row indicated an individual ROI, its category and x,y co-ordinates.
The two fluorescent channels, intersection mask and spreadsheet of annotated ROI co-ordinates were fed in to R. *k*-means clustering with estimated *k* was then performed as described above. The true positive rate and false positive rate were thus determined as the proportion of ROIs in each category that resided in the 'autofluorescence cluster', which was the cluster with highest average correlation values (**Supplementary Fig. 5 and 13**).

Code availability

This algorithm has been implemented with user interfaces in ImageJ, R and Matlab to accommodate the diverse image analysis community. The code and user documentation are available **https://ellispatrick.github.io/AFremover.**

Data availability

Data sets used in this study are available from the corresponding author upon reasonable request.

Ethics for use of human tissue samples

This study was approved by the Western Sydney Local Area Health District (WSLHD) Human Research Ethics Committee (HREC); reference number (4192) AU RED HREC /15 WMEAD/11. Human colorectal and skin tissues used for this study were approved by this committee. Brain and Heart tissue images were donated data.

Acknowledgements

We would like to acknowledge the Cell Imaging Core Facility at the Westmead Institute for their support and services. Also, Rashid F., member of the Chong Lab, for the rat heart images used for this study, and Bright F., for the human brain tissue images used for this study.

Also a special thanks to Cantrill L. for reviewing this manuscript. This work was funded by the National Health and Medical Research Council (Australia).

Author contributions

H.B conceived the project, collected data and wrote the first implementation of the algorithm. N.P.C wrote the majority of the codebase in ImageJ, MATLAB, and R. K.M.B, K.J.S, T.L.C., A.N.H and E.P were intellectual contributors to the project. All authors were involved in writing and editing the manuscript.

References:

1. Zrazhevskiy, P. & Gao, X. *Nat Commun* **4**, 1619 (2013).

2. Gerdes, M.J. et al. *Proceedings of the National Academy of Sciences* **110**, 11982–11987 (2013).

3. McKinley, E.T. et al. *JCI Insight* **2**, (2017).

4. Lin, J.-R., Fallahi-Sichani, M. & Sorger, P.K. *Nature Communications* **6**, 8390 (2015).

5. Sorger, P.K. et al. *eLife* **7**, e31657 (2018).

6. Gut, G., Herrmann, M.D. & Pelkmans, L. *Science* **361**, eaar7042 (2018).

7. Goltsev, Y. et al. *Cell* **174**, 968-981.e15 (2018).

8. del Castillo, P., Molero, M., Ferrer, J. & Stockert, J. *Histochemistry* **85**, 439–440 (1986).

9. Baschong, W., Suetterlin, R. & Laeng, H.R. *Journal of Histochemistry & Cytochemistry* **49**, 1565–1571 (2001).

10. Croce, A.C. & Bottiroli, G. *European Journal of Histochemistry* **58**, 2461 (2014).

11. Wizenty, J. et al. *Journal of immunological methods* **456**, 28–37 (2018).

12. Billinton, N. & Knight, A.W. *Analytical Biochemistry* **291**, 175–197 (2001).

13. Neumann, M. & Gabel, D. *Journal of Histochemistry & Cytochemistry* **50**, 437–439 (2001).

14. Davis, S.A. et al. *Journal of Histochemistry & Cytochemistry* **62**, 405–423 (2014).

15. Dickinson, M., Bearman, G., Tille, S., Lansford, R. & Fraser, S. *BioTechniques* **31**, 1272–1278 (2001).

16. Woolfe, F., Gerdes, M., Bello, M., Tao, X. & Can, A. *IEEE Transactions on Image Processing* **20**, 1085–1093 (2011).

17. Kim, M. et al. *PLOS Pathogens* **11**, e1004812 (2015).

18. Harman, A.N. et al. *Blood* **118**, 298–308 (2011).

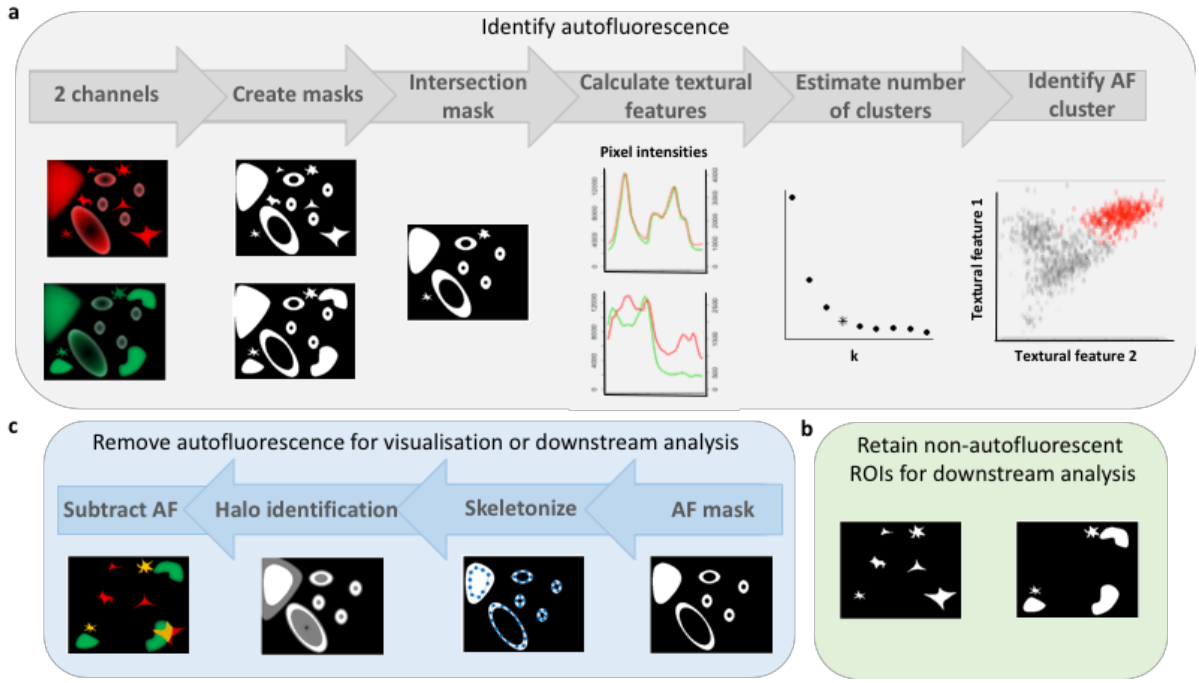

Fig. 1: Steps of the autofluorescence remover algorithm. a, *k-means* clustering on a set of textual features of objects in an intersection mask of two channels. Autofluorescent ROIs can then be tagged for exclusion in downstream analysis (**b**), or a custom dilation function can be employed to estimate the perimeter of autofluorescent ROIs, which are then digitally removed from the image (**c**).

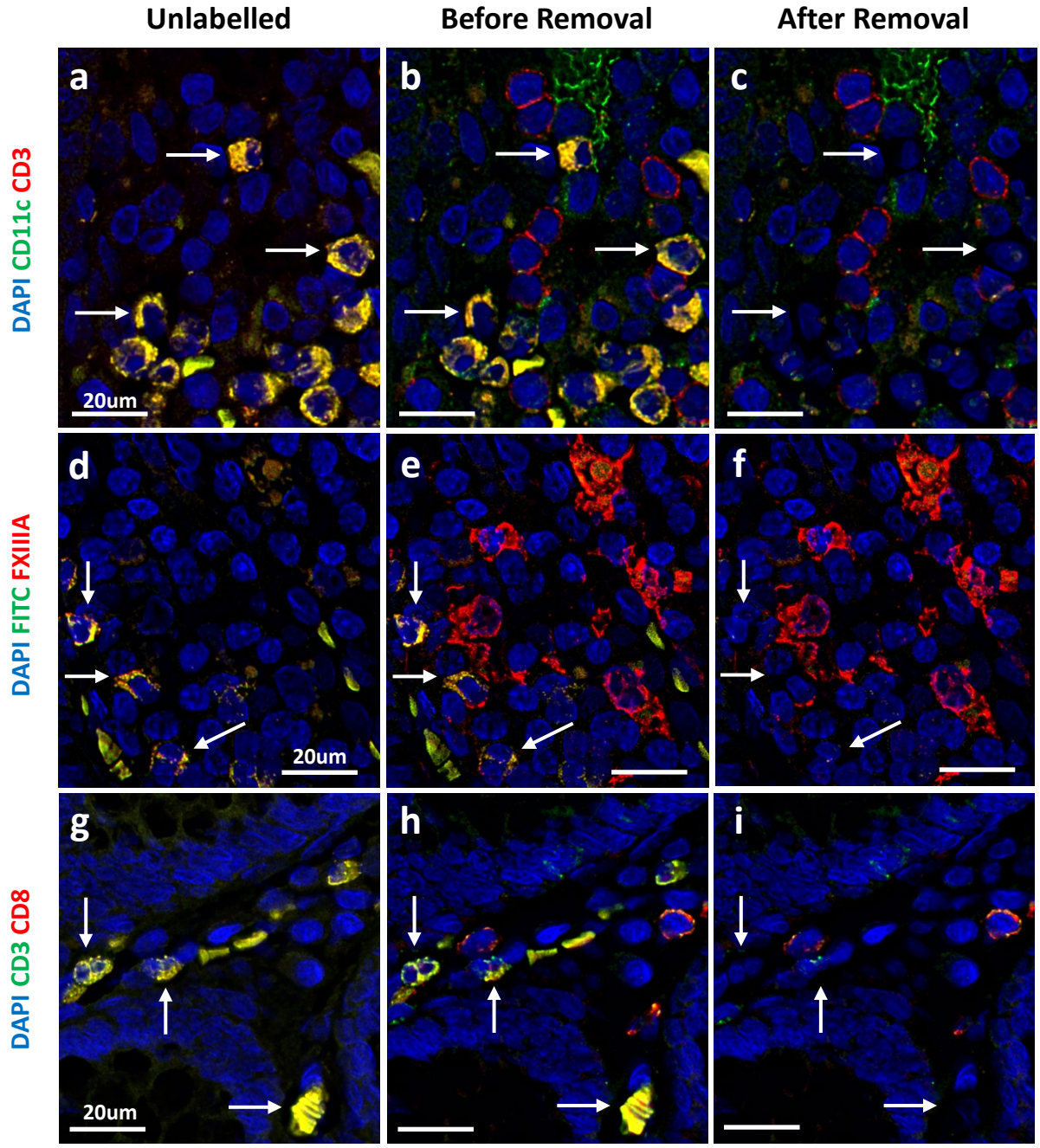

Fig. 2: Removal of autofluorescence from multiple staining panels. Sections of fixed human colorectal tissue prior to (**a,d,g**) and after labelling (**b,e,h**) with antibodies targeting the indicated markers. **c,f,i**, labelled images after autofluorescence removal. White arrows indicate some autofluorescent objects that have been removed by the algorithm. In the middle row 'FITC' is the FITC channel, which was imaged but not used to detect any markers. Images are representative of 3 donors for each staining panel.

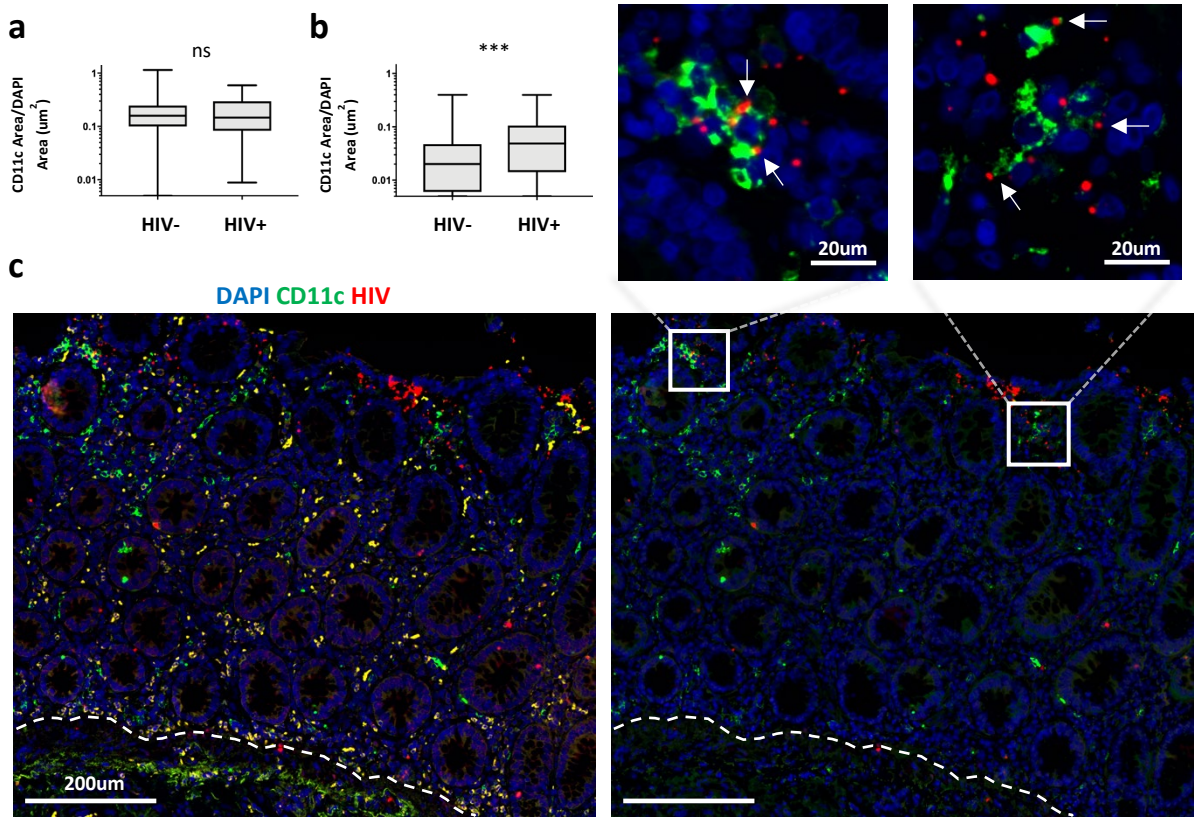

Fig. 3: Autofluorescence removal facilitates analysis of early HIV-target cell interaction. Human colorectal explants were topically infected with HIVBal for 30min, fixed, sectioned and then stained for CD11c, HIV RNA and DAPI. **a,b**, A whole tissue image from one donor was divided into 100x100um^2 quadrats, each classified as HIV- or HIV+, and CD11c labelling was measured before (a) and after (b) autofluorescence removal. CD11c expression was measured per um^2 of DAPI. Quadrats with DAPI staining less than 1/10th their area (non-tissue areas) were excluded. Boxplots show the min, first quartile, median, third quartile and max values. **c,** A cropped area of a whole-tissue image of HIV-infected colorectum before (left) and after (right) autofluorescence removal. Zoomed images of the boxes show interactions of HIV with CD11c+ cells (white arrows) in the image after autofluorescence removal. The broken white line indicates the base of the lamina propria. A two-tailed Mann Whitney test was performed in part **a** and **b**. ns = not significant; ***p=0.0002.

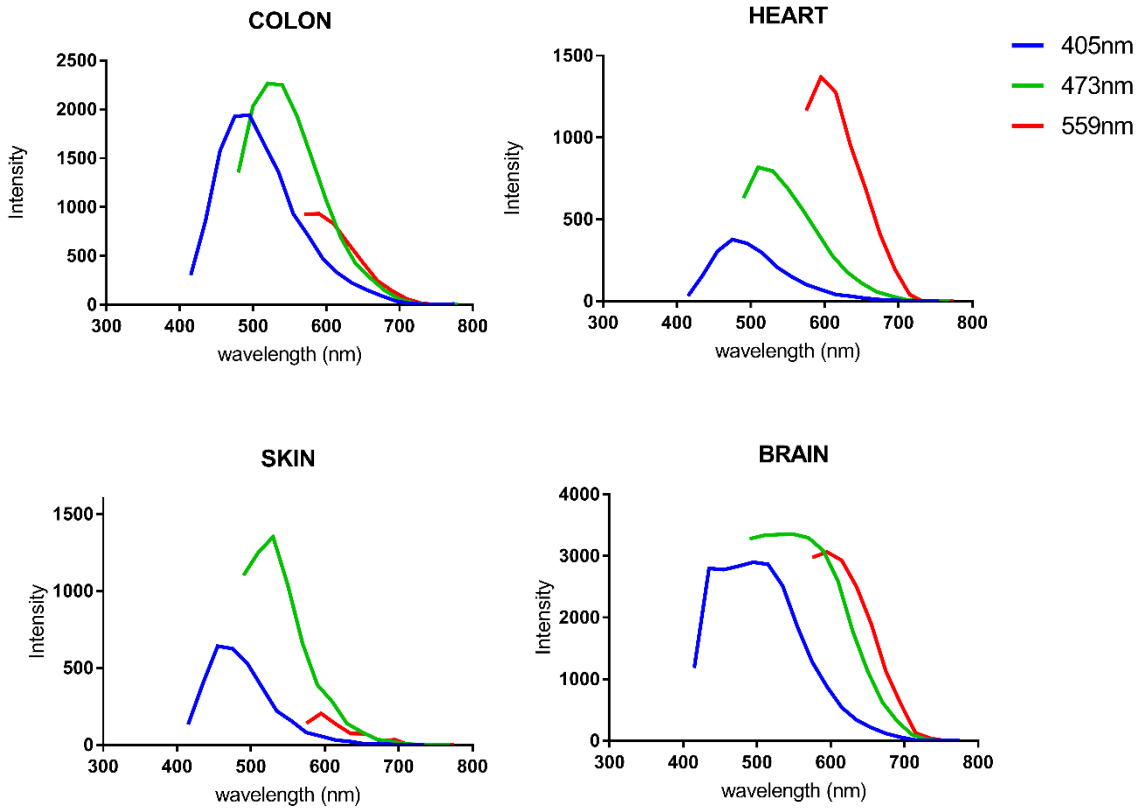

Supplementary Figure 1: Excitation and emission spectra of autofluorescence in various tissues. The intensity of pixels corresponding to autofluorescent structures measured at 20nm intervals upon excitation with laser lines 405nm, 473nm or 559nm in human colon, skin and brain tissues, as well as rat heart tissue. Results shown as the intensity of the autofluorescent object minus the intensity of the stromal background for each wavelength. Results are shown for a single image for each tissue type.

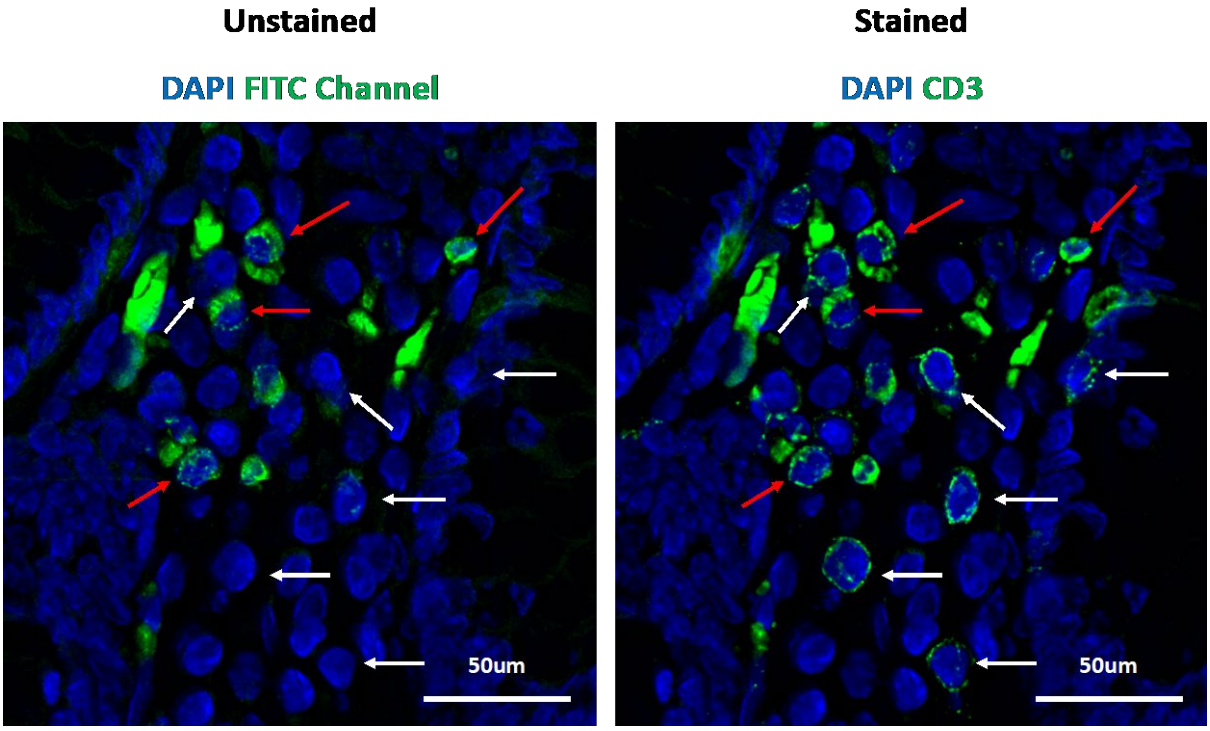

Supplementary Figure 2: Autofluorescence inhibits assessment of CD3 labelling in the human colorectum. Fixed human colorectal tissue sections imaged prior to (left) and after labelling with mouse anti human CD3 and donkey anti-mouse AF488 (right). Red arrows indicate some autofluorescent cells and white arrows indicate CD3+ cells. Images are representative of 6 unique donors where CD3 staining was performed.

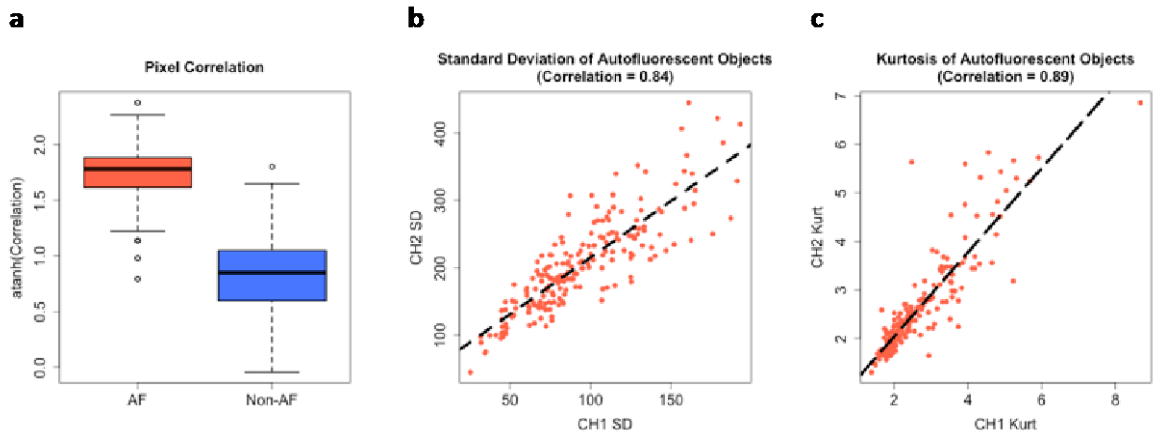

Supplementary Figure 3: Features of autofluorescence are highly correlated between fluorescent channels. Fixed human colorectal tissue sections were stained for mouse anti CD3 and and rabbit anti CD4, detected using donkey anti-mouse AF488 and donkey anti-rabbit AF546 respectively. An intersection mask was created using the two fluorescent markers (**Fig. 1**) and measurements performed on objects in the intersection mask. An unstained background image was used as a reference to manually annotate autofluorescent objects in the stained image. **a**, The arctanh transformed Pearson's correlation coefficient values of autofluorescent objects vs non-autofluorescent objects within the intersection mask. The boxplots contain data from thousands of individual objects for each category. **b,c**, standard deviation and kurtosis measurements of autofluorescent objects in each channel used to create the intersection mask. A subsample of 200 autofluorescent objects, among thousands, is shown. These graphs are representative of 13 total images used for this work.

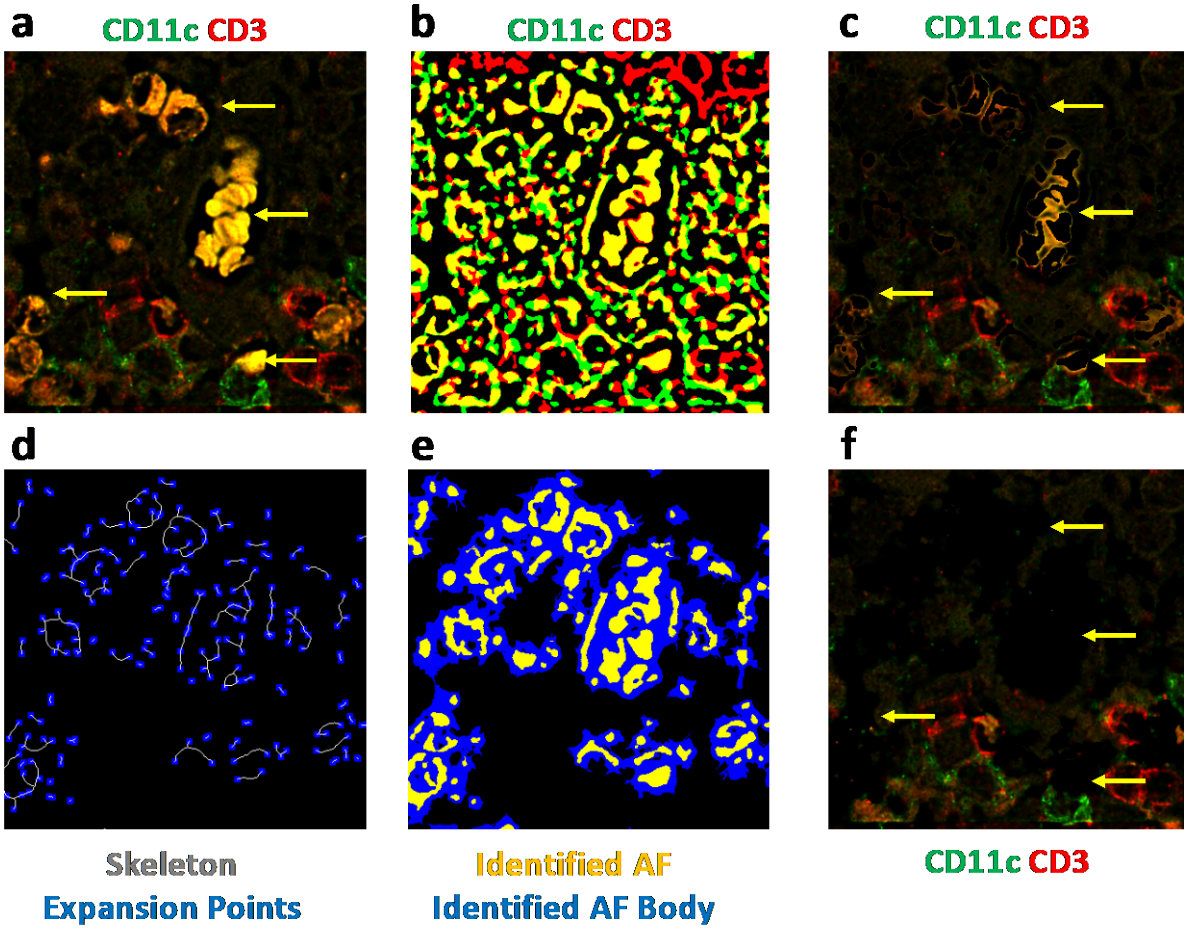

Supplementary Figure 4: Custom dilation function to estimate the correct perimeter of autofluorescent ROIs. a, Fixed colorectal tissue sections were stained for rabbit CD11c and mouse CD3, followed by donkey anti rabbit AF488 and donkey anti mouse AF546. **b**, Fluorescent channels used to detect CD11c and CD3 were thresholded, binary masks created and the composite image displayed. Yellow indicates the overlapping area corresponding to the intersection mask. **c**, Image from part a with the pixels in the intersection mask from part b set to 0. **d**, Identified autofluorescent objects within the intersection mask in part b are skeletonised and points for outward expansion (blue) are distributed along the skeleton every 20 pixels. **e**, Thousands of equiangular lines are drawn outwards from the expansion centres identified in part d, each line propagating until it encounters a pixel brighter than the previous pixel, as measured in either the CD11c or CD3 channel. A mask of the identified autofluorescence body is thus generated for each fluorescent channel. **f**, Pixels corresponding to the identified AF body in each channel in part e, are set to 0. Yellow arrows indicate some autofluorescent objects.

a

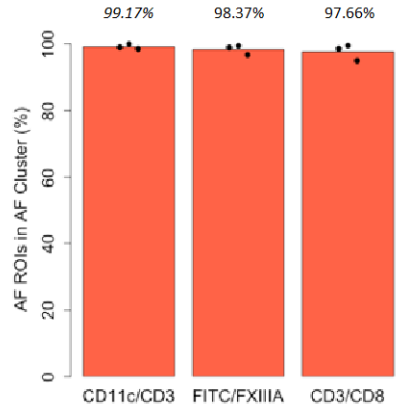

b

Case	Identified AF/Total AF	Identified Real Signal/Total Real Signal	Number of ROIs	Number of AF ROIs
CD11c/CD3	198/198	3/142	15904	1954
CD11c/CD3	182/199	0/193	34298	1373
CD11c/CD3	199/200	2/197	26287	1272
FITC/Mac	207/210	7/181	23456	3552
FITC/Mac	189/204	2/197	21552	2003
FITC/Mac	176/197	1/208	16442	1179
CD3/CD4	199/201	1/205	21355	2111
CD3/CD4	187/198	10/189	20310	1452
CD3/CD4	206/207	3/202	63997	3571

Supplementary Figure 5: Specificity and sensitivity of autofluorescence removal for various use-cases in Figure 2. Fixed human colorectal sections were imaged prior to, and after labelling with antibodies against markers for three separate panels, CD11c/CD3, FITC/FXIIIA and CD3/CD4. FITC indicates an unstained open channel that was imaged. An intersection mask was created using the two fluorescent channels for each panel (as in Figure 1). Textural features of objects within the intersection mask were then measured for each channel, including standard deviation, kurtosis, as well as the inter-channel Pearson's correlation coefficient of corresponding pixels. *k*-means clustering was then performed using these features and the cluster with the highest average correlation values was defined as the cluster containing autofluorescent ROIs. A ground truth for the classification of objects as autofluorescence or real signals (stemming from antibodies) was established by manually annotating a subset of up to 200 ROIs each, using the unlabelled background image as a reference. **a**, percentage of the 'autofluorescence cluster' comprised of autofluorescent ROIs (specificity), where the total number of ROIs in the cluster is defined as the sum of autofluorescent ROIs and ROIs stemming from real signal. Each data point represents counts performed on a unique donor for each panel. Mean values across the three donors are indicated above each column. **b**, table summarising the proportion of manually annotated autofluorescence or real signal assigned to the 'autofluorescence cluster' (sensitivity). The last two columns indicate the total number of ROIs and the total number of ROIs classified as autofluorescence respectively. Each row corresponds to results for unique donors for each use-case.

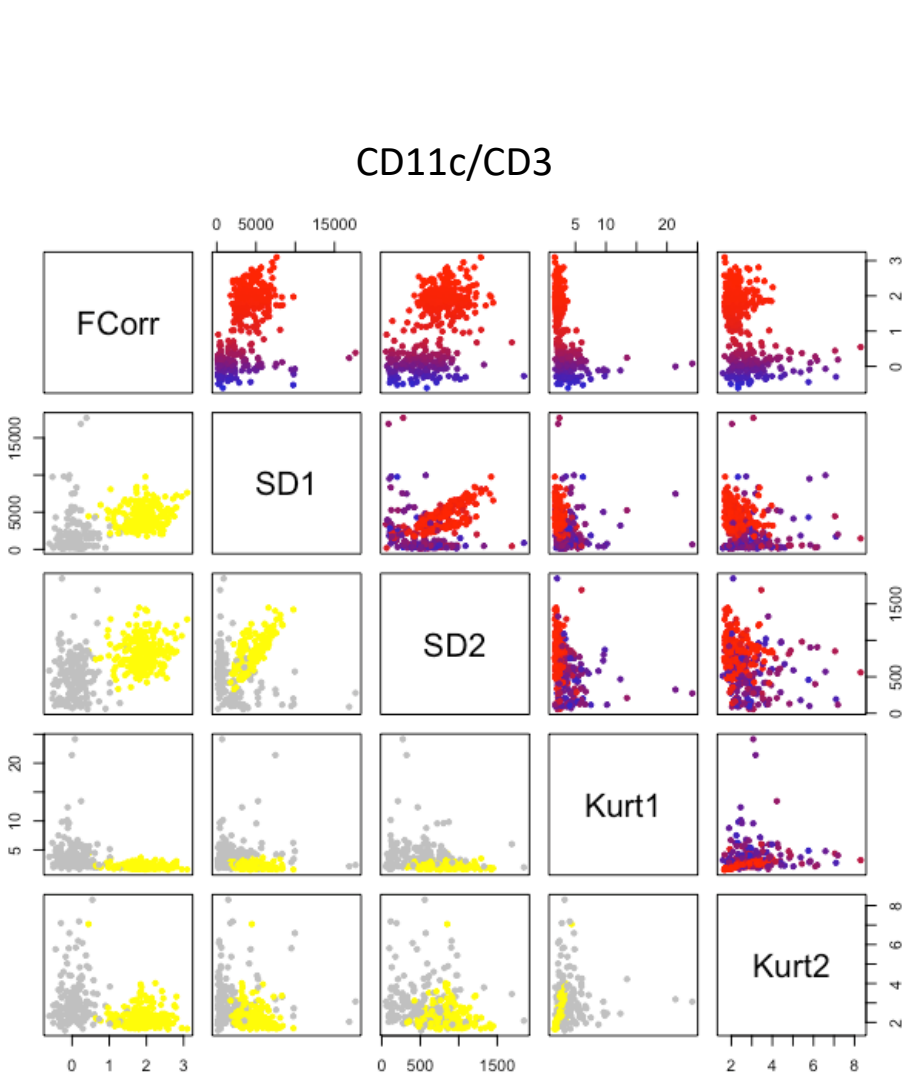

Supplementary Figure 6: Pairwise plots of textural features used for *k*-means clustering of the non-co-expressed markers use-case. ROIs from *k*-means clustering on the CD11c/CD3 use-case in Supplementary Figure 5 are shown. In the bottom half, ROIs in the autofluorescence cluster are coloured yellow, whilst non-autofluorescent ROIs (real signal + dim stromal background fluorescence) are coloured grey. The top half shows paired plots as a heatmap of correlation values. FCorr = Arctanh transformed Pearson's correlation coefficient values. SD1, SD2, Kurt1, Kurt2 = Standard deviation or Kurtosis values of ROIs in channels 1 or 2. The plot is representative of clustering performed on 3 independent donors.

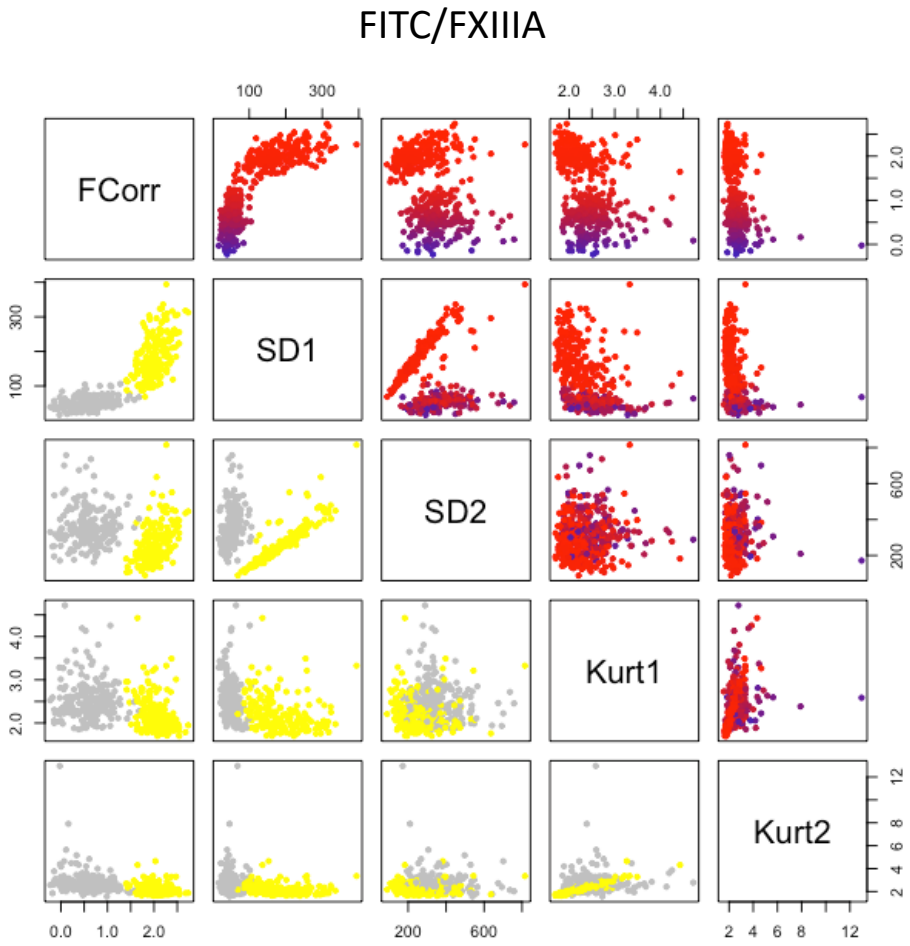

Supplementary Figure 7: Pairwise plots of textural features used for *k*-means clustering of the autofluorescent cells use-case. ROIs from K-means clustering on the FITC/FXIIIA use-case in Supplementary Figure 5 are shown. In the bottom half, ROIs in the autofluorescence cluster are coloured yellow, whilst non-autofluorescent ROIs (real signal + dim stromal background fluorescence) are coloured grey. The top half shows paired plots as a heatmap of correlation values. FCorr = Arctanh transformed Pearson's correlation coefficient values. SD1, SD2, Kurt1, Kurt2 = Standard deviation or Kurtosis values of ROIs in channels 1 or 2. The plot is representative of clustering performed on 3 independent donors.

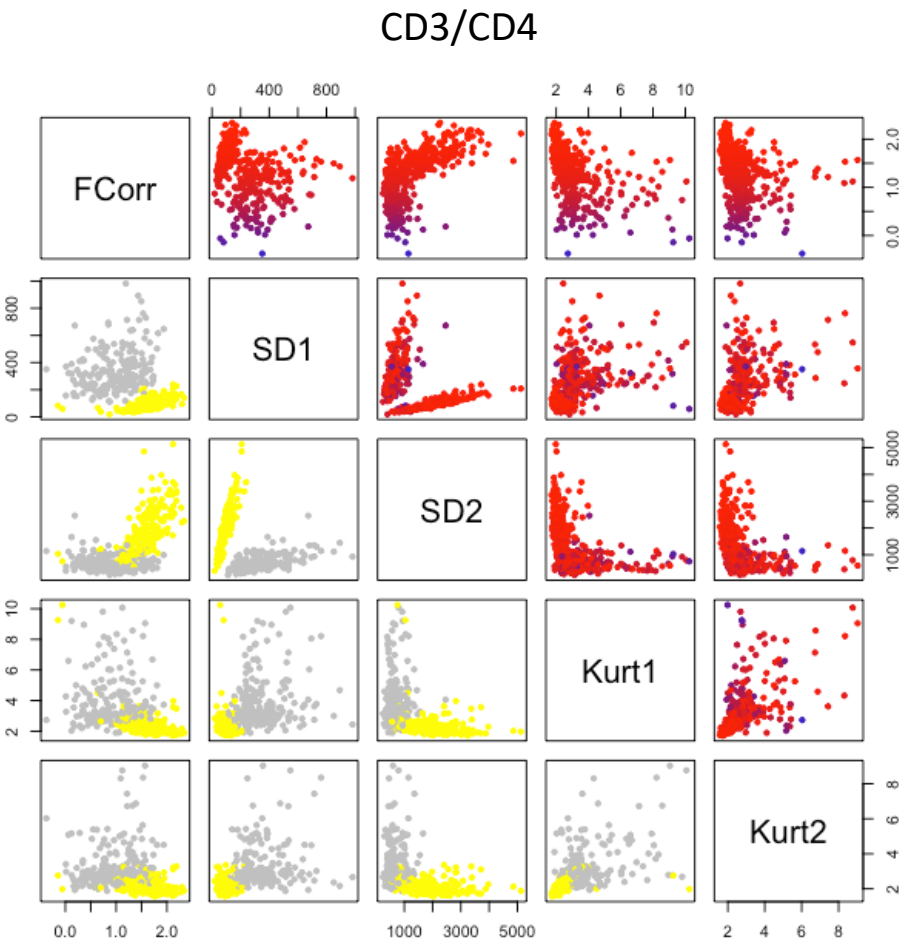

Supplementary Figure 8: Pairwise plots of textural features used for *k*-means clustering of the co-expressed markers use-case. ROIs from K-means clustering on the CD3/CD4 use-case in Supplementary Figure 5 are shown. In the bottom half, ROIs in the autofluorescence cluster are coloured yellow, whilst non-autofluorescent ROIs (real signal + dim stromal background fluorescence) are coloured grey. The top half shows paired plots as a heatmap of correlation values. FCorr = Arctanh transformed Pearson's correlation coefficient values. SD1, SD2, Kurt1, Kurt2 = Standard deviation or Kurtosis values of ROIs in channels 1 or 2. The plot is representative of clustering performed on 3 independent donors.

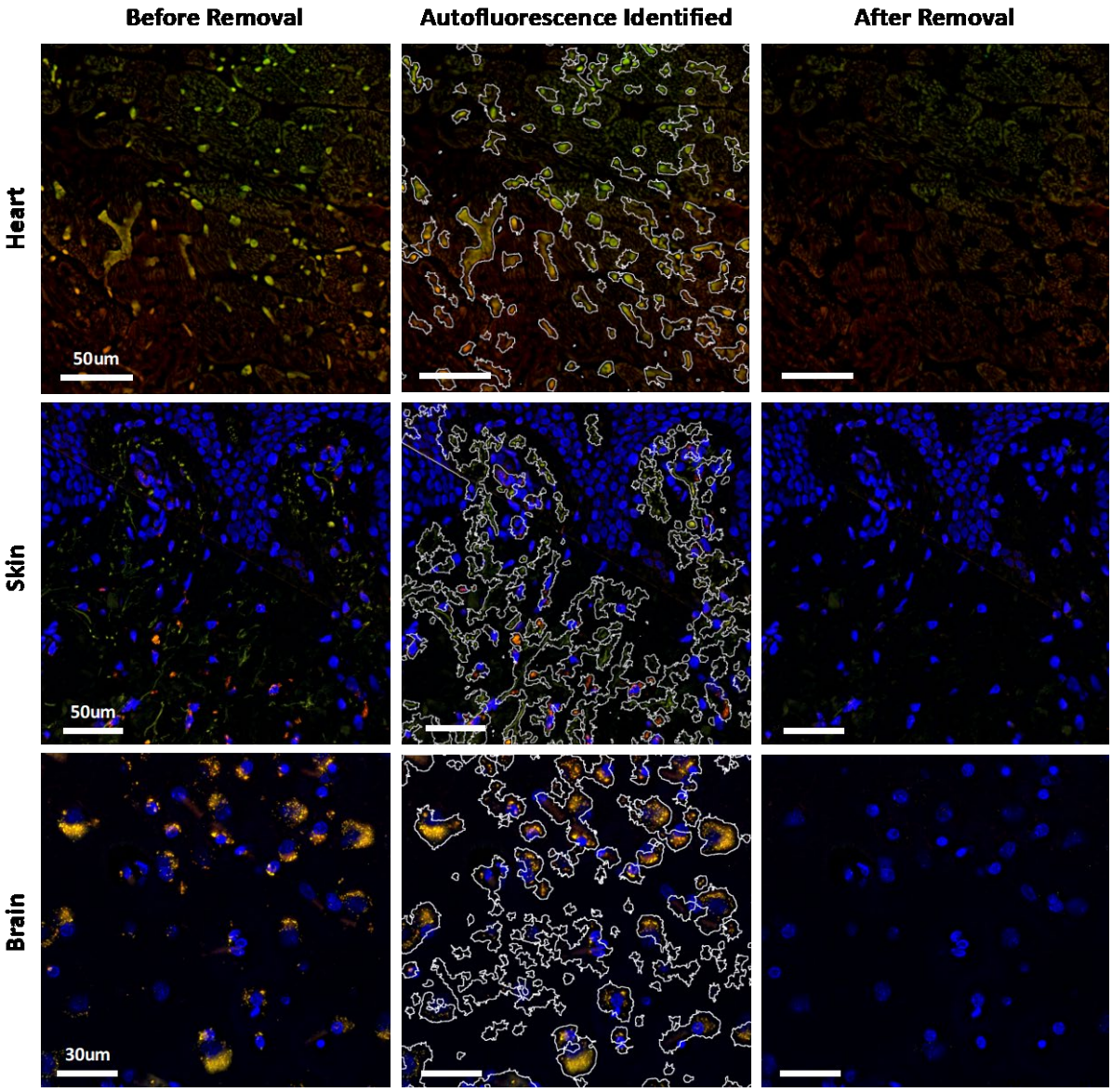

Supplementary Figure 9: Autofluorescence removal on various tissue types. Unlabelled sections of fixed rat heart, human abdominal skin and human brain tissue are shown, prior to autofluorescence removal (left panel), with the boundary of autofluorescent structures identified by the algorithm (middle panel), and after setting pixel values to 0 (right panel). Note that the images the skin and brain samples were counterstained with DAPI for visualisation. The images are representative areas from one whole-tissue image for each tissue type that was used for autofluorescence removal.

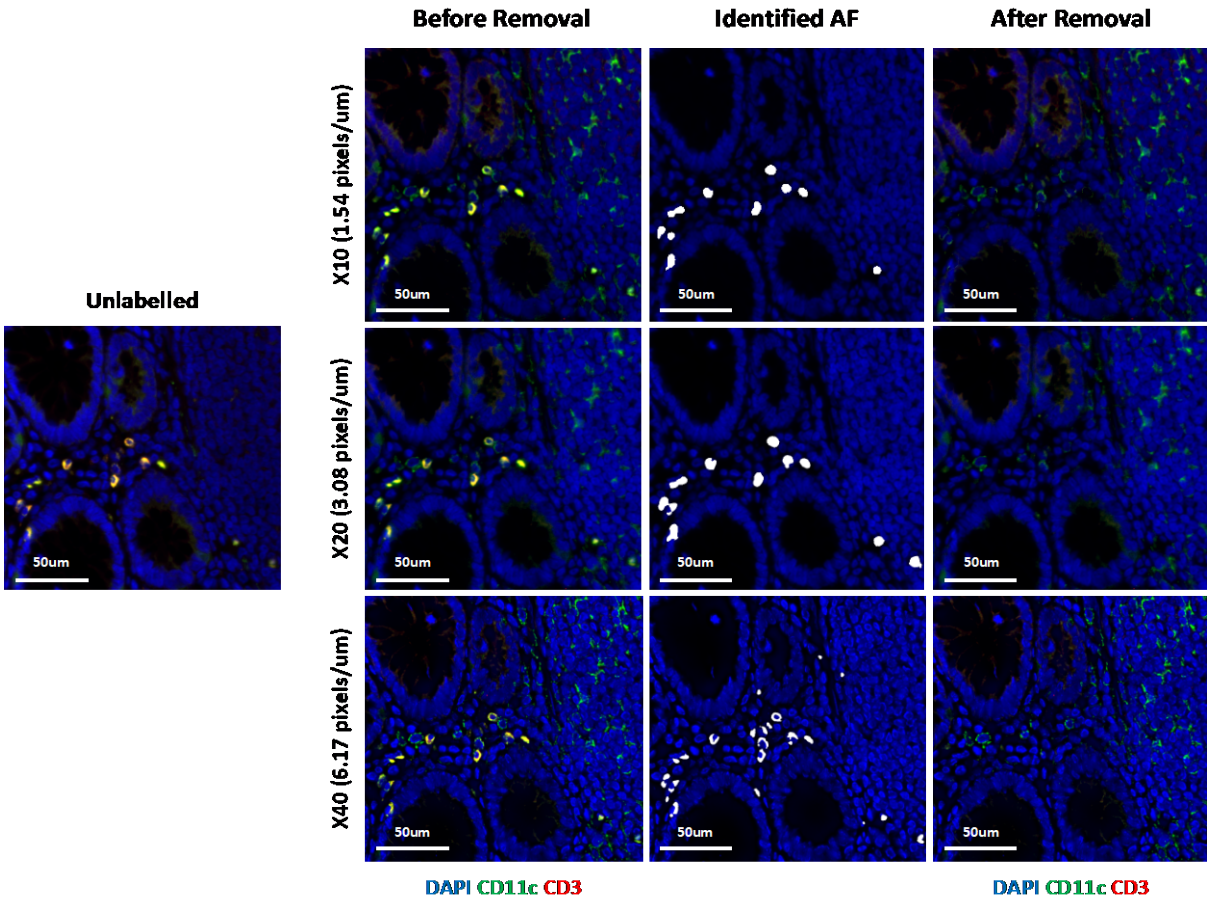

Supplementary Figure 10: Autofluorescence removal at varying image resolutions. Fixed colorectal tissue sections were imaged prior to labelling (left, unlabelled image) and after labelling for rabbit anti CD11c and mouse anti CD3, followed by donkey anti rabbit AF488 and donkey anti mouse AF546. Images of the same area were taken with x10, x20 and x40 objectives with an image resolution of 1.54, 3.08 and 6.17 pixels per um respectively. Images before autofluorescence removal (left panel), with a mask of the identified autofluorescence overlaid (middle panel) and after removal by setting pixel values to 0 (right panel) are shown. Images are representative of 3 unique donors where CD11c/CD3 staining was carried out and imaged at various magnifications.

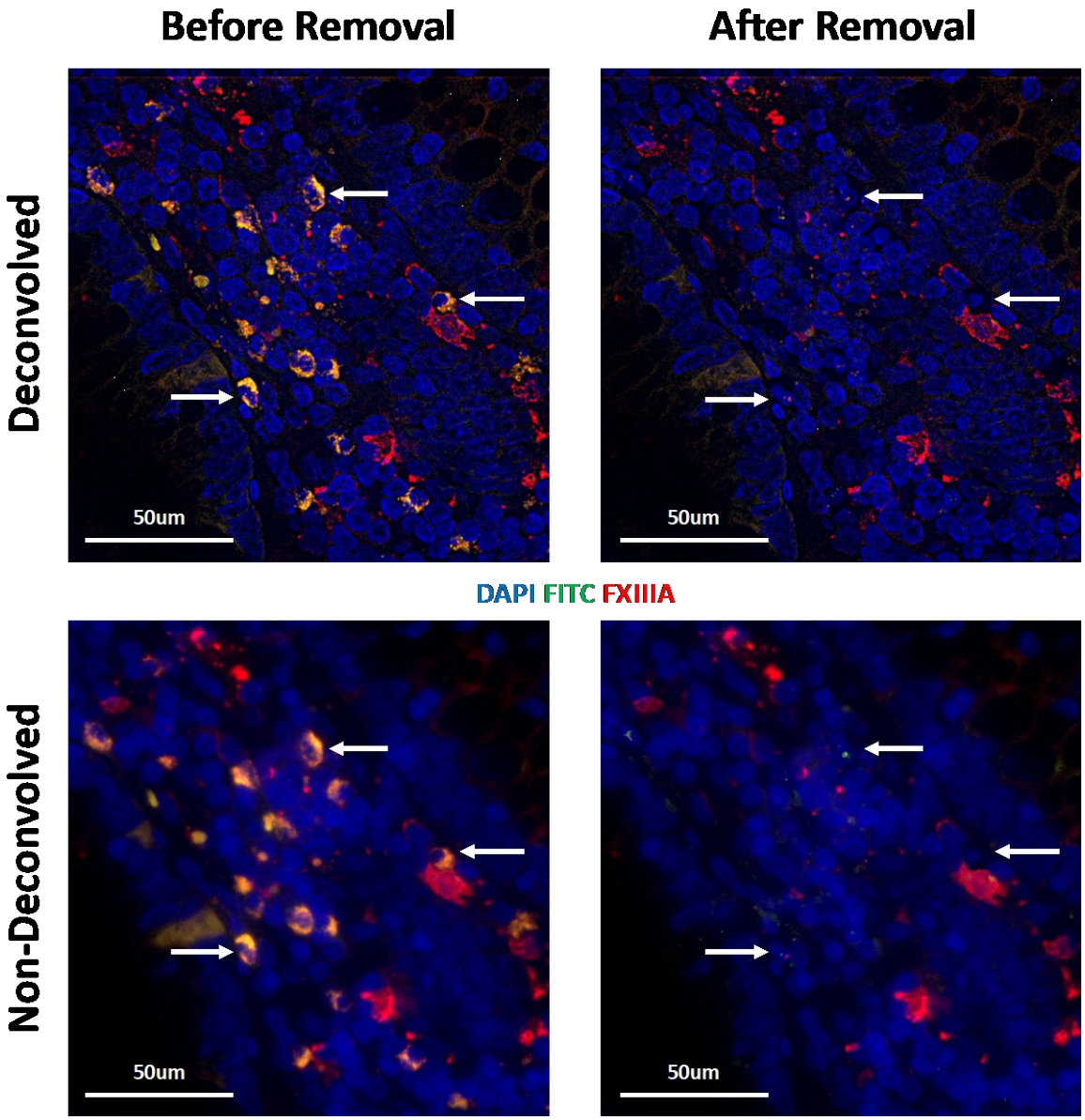

Supplementary Figure 11: Autofluorescence removal before and after deconvolution. Fixed colorectal tissue sections were labelled with a sheep anti FXIIIA antibody followed by donkey anti sheep AF546. 'FITC' is the FITC channel, which was imaged but not used to detect any markers. Images are shown of the same area before (bottom row) and after (top row) deconvolution using Huygens deconvolution software, CMLE algorithm. Images before (left panel) and after (right panel) autofluorescence removal are shown. White arrows indicate some autofluorescence removed by the algorithm. Images are representative of 3 unique donors stained for FXIIIA and processed for autofluorescence removal before and after deconvolution.

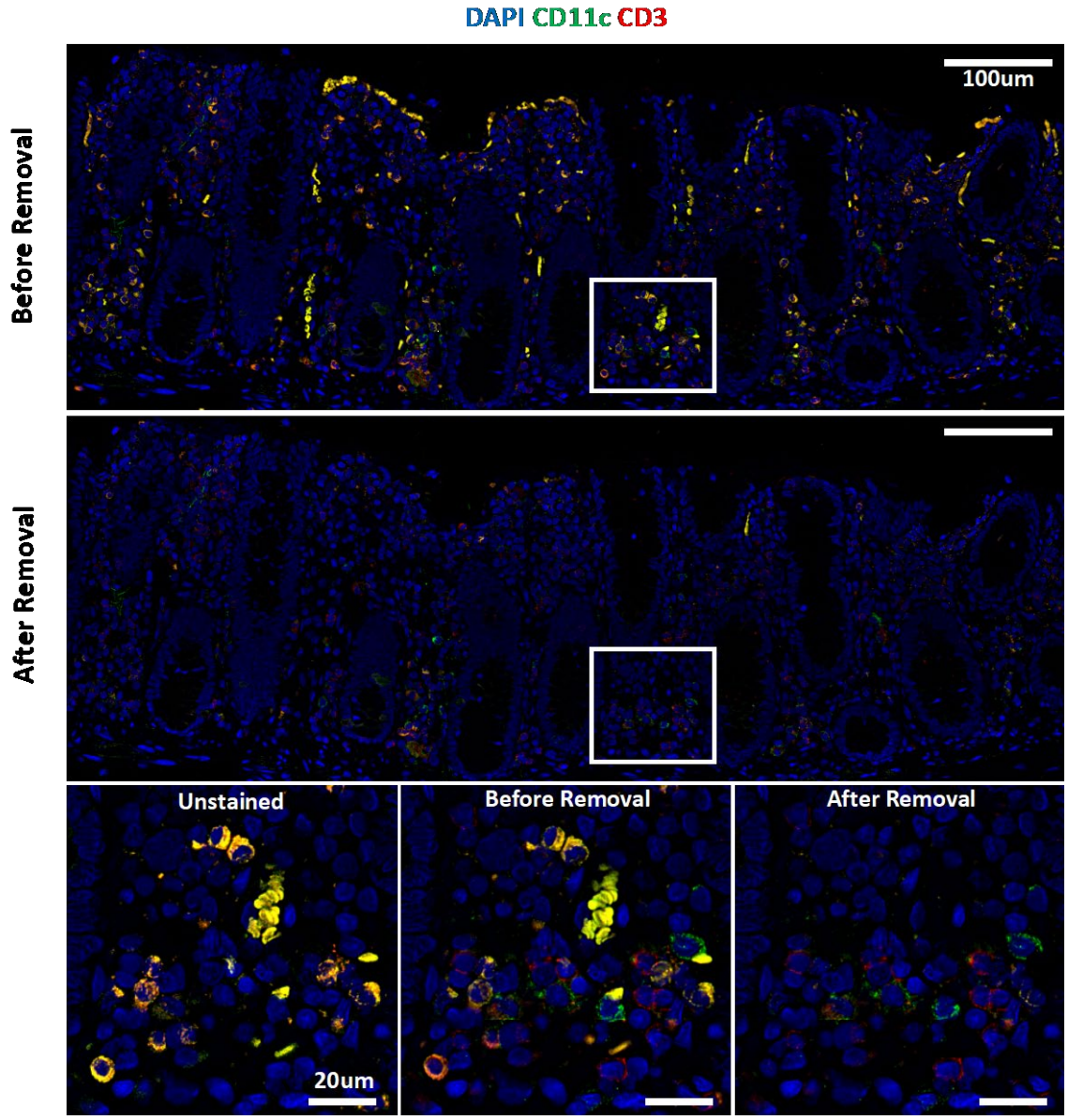

Supplementary Figure 12: Autofluorescence removal on large images. Fixed colorectal tissue sections were imaged prior to and after labelling for rabbit anti CD11c and mouse anti CD3 antibodies, followed by donkey anti rabbit AF488 and donkey anti mouse AF546. A large area of tissue was imaged and the results before (top panel) and after (middle panel) autofluorescence removal are shown. Zoomed in images of the area outlined are shown with an additional image of the unlabelled section outlining the distribution of autofluorescence. Image is representative of 3 unique donors where CD11c/CD3 staining was carried out.

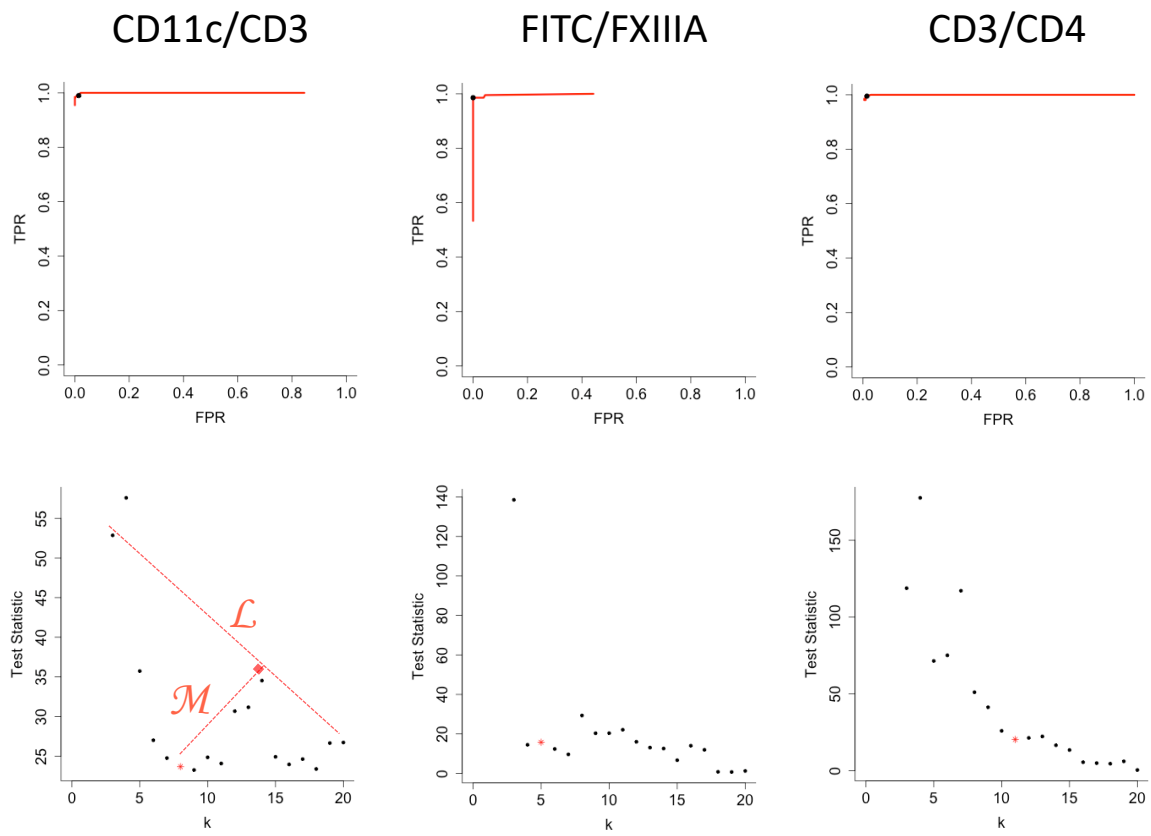

Supplementary Figure 13: Estimation of optimal cluster number for *k*-means. *k*-means clustering as described in supplementary figure 5 was performed iteratively for 3-20 clusters and the distribution of paired true positive rate (TPR) and false positive rate (FPR) values for each cluster number is indicated by the red line for each use-case (top row). A high TPR or FPR corresponds to a high proportion of the 'autofluorescence cluster' comprising manually annotated autofluorescence or real signals respectively. The bottom row shows plots of the cluster number *(k)* versus, test statistic of a t-test (two-tailed) comparing Pearson's correlation coefficient values of clusters with the highest ('autofluorescence cluster') and second highest average correlation values. An elbow method approach for estimation of optimal K is illustrated in the bottom left plot. A line (L) is drawn between the first and last plotted values. The line M indicates the plotted value that is below the line L, and has the greatest perpendicular distance to that line. The cluster number corresponding to this plotted point is estimated as the optimal cluster number. The points with optimal cluster number for each plot are indicated as a red *. The TPR/FPR of the optimal cluster number for each use-case is indicated by the black dot in the top row of plots. Data are representative of analysis performed on 3 unique donors for each use-case.